

Cite this: *J. Mater. Chem. A*, 2023, **11**, 12928

# Probing single-chain conformation and its impact on the optoelectronic properties of donor–accepter conjugated polymers†

Zhiqiang Cao, <sup>‡a</sup> Zhaofan Li, <sup>‡b</sup> Sara A. Tolba, <sup>c</sup> Gage T. Mason,<sup>d</sup> Miao Xiong, <sup>e</sup> Michael U. Ocheje, <sup>d</sup> Amirhadi Alesadi,<sup>b</sup> Changwoo Do, <sup>f</sup> Kunlun Hong, <sup>g</sup> Ting Lei, <sup>e</sup> Simon Rondeau-Gagné, <sup>d</sup> Wenjie Xia <sup>\*b</sup> and Xiaodan Gu <sup>\*a</sup>

The chain conformation of donor–acceptor conjugated polymers (D–A CPs) is critical to their optical and electronic properties. However, probing the conformation of D–A CPs (e.g., persistence length and contour length) at a single-chain level is challenging due to the formation of aggregates in dilute solution, even in a good solvent. In this work, we studied the chain conformation and corresponding optical spectra for high-performance D–A CPs in the single-chain state by multimodal variable-temperature scattering and spectroscopy techniques, as well as by molecular dynamics simulations. We found a critical role of the side-chain length and branch point in the persistence length and optical absorption due to steric effects. Hence, it is important to consider both the chain rigidity and coplanarity of the polymer backbone to achieve desirable optoelectronic properties. Our findings bridge the fundamental knowledge gaps to design new CPs with desired optoelectronic properties *via* molecular engineering for next-generation electronic devices.

Received 2nd December 2022  
Accepted 14th February 2023

DOI: 10.1039/d2ta09389h

rsc.li/materials-a

## 10th anniversary statement

The *Journal of Materials Chemistry* family is a leading material journal for functional materials for energy research. As a student, I was greatly inspired by many studies published in those journals throughout my doctoral and postdoctoral studies. As an independent researcher, there are many great opportunities offered as well, such as the “Emerging Investigator themed issue”. Such a platform gives those who are just starting out an excellent opportunity to engage with this fantastic journal and provide great support to newbie faculties. On the occasion of the 10 year anniversary, I wish that the RSC journal continues to lead the pack as the go-to publisher for functional materials for energy research.

## 1. Introduction

Semiconducting conjugated polymers (CPs) have already seen wide usage in applications of organic field-effect transistors

(OFETs),<sup>1–4</sup> organic photovoltaics (OPVs),<sup>5–11</sup> and organic light-emitting diodes (OLEDs),<sup>12</sup> due to their flexibility, solution processability, and tuneable optical and electronic properties.<sup>13–16</sup> Various materials, in particular donor–acceptor (D–A) CPs composed of alternating electron-rich (donors) and electron-poor (acceptors) moieties within the polymer backbone, have been extensively studied due to their excellent optoelectronic properties.<sup>17</sup>

Chain conformation (*i.e.*, chain rigidity and local backbone planarity) dictates the delocalized electron cloud along the polymer backbone, which greatly influences the optical and electronic properties of CPs. Chain rigidity is often quantified by the persistence length ( $l_p$ ), also known as the characteristic length for the exponential decay of the correlations of backbone tangents.<sup>18</sup> The  $l_p$  is typically believed to be the upper limit for the conjugation lengths.<sup>19</sup> Theoretical studies by Troisi *et al.*<sup>20</sup> showed that the charge carrier mobility rises with increasing  $l_p$  as carriers can travel further on an individual chain. CPs with a longer  $l_p$  also possess higher photoluminescence quantum

<sup>a</sup>School of Polymer Science and Engineering, The University of Southern Mississippi, Hattiesburg, MS 39406, USA. E-mail: xiaodan.gu@usm.edu

<sup>b</sup>Department of Civil, Construction, and Environmental Engineering, North Dakota State University, Fargo, ND 58108, USA. E-mail: wenjie.xia@ndsu.edu

<sup>c</sup>Materials and Nanotechnology Program, North Dakota State University, Fargo, ND, 58102, USA

<sup>d</sup>Department of Chemistry and Biochemistry, Advanced Materials Centre of Research (AMCORE), University of Windsor, Windsor, Ontario, N9B3P4, Canada

<sup>e</sup>School of Materials Science and Engineering, Peking University, Beijing 100871, China

<sup>f</sup>Neutron Scattering Division, Oak Ridge National Laboratory, Oak Ridge, TN 37831, USA

<sup>g</sup>Center for Nanophase Materials Sciences, Oak Ridge National Laboratory, Oak Ridge, TN 37831, USA

† Electronic supplementary information (ESI) available. See DOI: <https://doi.org/10.1039/d2ta09389h>

‡ These authors contributed equally to this work.

yield<sup>21</sup> and optical absorption.<sup>22</sup> While small-angle X-ray or neutron scattering (SAXS/SANS) is a powerful technique for quantifying the  $l_p$  of a polymer chain, the accurate determination of the single-chain conformation of D–A CPs is non-trivial and requires a careful interpretation due to the existence of aggregates. The formation of aggregates is evidenced by the low  $q$  scattering upturn,<sup>23–25</sup> additional low-energy vibronic progression in spectroscopy,<sup>26,27</sup> and the appearance of new chemical shifts in the nuclear magnetic resonance (NMR) spectra.<sup>26</sup> The existence of aggregates that contain few polymer chains leads to an overestimation of the chain rigidity. For example, Wang *et al.*<sup>23</sup> found that poly[3,6-bis(5-thiophen-2-yl)-2,5-bis(2-octyldodecyl) pyrrolo [3,4-c]pyrrole1,4(2*H*,5*H*)-dione-2,2'-diyl-alt-thieno[3,2-*b*]thiophen-2,5-diyl] (DPPDIT) in chloroform exhibits rod-like conformation, while the scattering curve didn't show a Guinier region. Also, many other papers focused on aggregates of D–A CPs only.<sup>28–30</sup> Even though there are a couple of studies aimed at determining the chain conformation of D–A CPs by interpreting the scattering profiles using a complex combined model,<sup>23,25,31</sup> accurate understanding of chain conformation is challenging due to the excessive number of parameters/variables that need to be fitted, as well as a weak scattering signal from dissolved chains since the scattering intensity scales with scattering objects. Nevertheless, the Pozzo group<sup>31</sup> used a combined model consisting of a parallelepiped model for nanoribbon aggregates and a flexible cylinder model for dispersed chains to fit SANS of D–A polymers such as DPPDIT in poor solvent. They extracted a  $l_p$  of 15 nm for DPPDIT. More recently, Diao *et al.*<sup>25</sup> used two flexible cylinder models, one for single chains and the other for fibril aggregates, to fit SAXS of isoindigo-bithiophene-based polymer (PII-2T) in poor solvent and got a  $l_p$  of 7.5 nm for PII-2T. Thus, key limitations in the current studies include the overfitting of scattering data, which induces inconsistencies of single chain conformation between the reported studies.<sup>25</sup>

The aggregation formation of D–A CPs is highly temperature-dependent.<sup>23,29</sup> However, as far as we know, temperature-dependent SAXS/SANS has rarely been used for characterizing D–A CP solutions, and the majority of experiments were done at room temperature.<sup>32</sup> Wang *et al.*<sup>23</sup> monitored the solution structure during heating DPPDIT solution (in deuterated orthodichlorobenzene) by temperature-dependent SANS. DPPDIT can only dissolve at high temperatures (above 130 °C), as indicated by a Guinier region in a low scattering vector region. Recent temperature-dependent SAXS studies by Toney *et al.*<sup>29</sup> and SANS studies by our group<sup>24</sup> showed the temperature-dependent aggregation of quaterthiophene-cobenzothiadiazole (difluorinated) polymers (PffBT4T). The underutilized temperature-dependent scattering has left fundamental gaps in our knowledge of the structure–conformation relationships within D–A CPs, practically in a fully dissolved single chain state.

The chain rigidity of CPs is primarily determined by the backbone deflection angles and torsional angles.<sup>32</sup> Thus, co-linear conjugated units, extended conjugated units, and torsion-resistant linkages would allow for rigid CPs. The community has used this guidance to develop several new CPs

with increased chain rigidity by introducing extended, fused-ring conjugated units.<sup>22,33</sup> Several groups also suggested that torsion-free ladder-type CPs<sup>34</sup> and double-bond linked fused-ring CPs<sup>35</sup> could further enhance the backbone rigidity and consequently improve device performance. Nevertheless, a planar backbone does not always mean a high chain rigidity. Recently, Venkateshvaran *et al.* reported that although IDTBT polymers possess a highly local planar backbone, which enables a high charge carrier mobility, the polymer chain adopts a wavy backbone rather than a planar rigid rod.<sup>33</sup> Another good example is poly(3-hexylthiophene) (P3HT). While both coplanar conformations (*cis* conformation and *trans* conformation) preserve the  $\pi$ -conjugation, the *cis* conformation induces backbone kinks, resulting in a more flexible chain.<sup>36</sup> For more complex donor and acceptor polymers, different building blocks along the polymer backbone can be distorted to form a torsional angle in the ground energy state as revealed by the density functional theory (DFT) technique. Thus, there is a need to investigate both the chain rigidity and local backbone planarity of D–A CPs and understand their impact on optoelectronic properties.

Side chains influence the chain conformation by affecting dihedral potentials between different building blocks due to steric effects.<sup>36–39</sup> So far, the role of side chains on CP's  $l_p$  remains controversial.<sup>40</sup> For polythiophenes, poly(3-dodecylthiophene) (P3DDT) with larger alkyl side chains showed a significantly lower  $l_p$  than P3HT in solution, at 1 nm *versus* 3 nm, respectively.<sup>36</sup> The decreased  $l_p$  is due to conformational twisting of the conjugated backbone arising from stronger steric repulsion of neighboring side chains. In contrast, the larger alkyl side chains of cyclopentadithiophene-co-pyridalithiadiazole polymers (PCPDPT)<sup>32</sup> and PffBT4T<sup>24</sup> induced a higher  $l_p$ . Unfortunately, current experimentally reported  $l_p$  for D–A CPs is limited,<sup>23,31,41</sup> which hinders the understanding of the chain conformation of D–A CPs, not to mention its impact on optoelectronic properties.

In addition to experimental quantification, the capability to predict chain conformation using computational approaches has recently been evolved to facilitate the understanding on CP's chain conformation. All-atomistic molecular dynamics (AA-MD) simulations can simulate the behavior of polymer chains by building a long-chain polymer model and provide an understanding of the experimentally observed chain conformation at the molecular level.<sup>42</sup> De Pablo *et al.* integrated experimental characterization of PTB7 by SANS measurements and AA MD simulations, where  $l_p$  values from both approaches agreed.<sup>41</sup> First-principles calculations have also been widely used in predicting the optimal conformations and electronic structure of CPs. For example, Jackson *et al.* found that diverse nonbonding interactions between the adjoining donor and acceptor units can enhance the backbone planarity.<sup>43</sup> Despite tremendous progress, to date, a detailed study of the structure–conformation–property relationships of D–A CPs through an integrated experimental and computational approach has not been reported yet.

In this work, we combined experimental and computational approaches to provide first in depth understanding of the side

alkyl chain's influence on backbone conformation and their optoelectronic properties. We found a critical role of the side-chain length and side-chain branching point position in the  $l_p$  for high-performance diketopyrrolopyrrole (DPP) and isoindigo (IID) based polymers. We discovered that although the chain rigidity of DPP-based polymers increased with the side-chain length due to decreased population in *cis* conformation between thiophene units, blue shifts in the absorption spectrum were observed. DFT calculations of the backbone planarity and optical absorption unraveled that the blue shifts can be attributed to the less planar backbone. The  $l_p$  of IID-based polymers increased when moving the branching position farther away from the backbone due to the decreased *cis* conformation. However, the optical shift for IID-based polymers changed according to an odd-even effect of the branching point, which can be ascribed to the coplanarity change of the polymer backbone due to the steric hindrance induced by side chains according to DFT calculations. Our findings emphasized the importance of side chains in controlling the single chain conformation of D–A CPs through the local torsional angle along the backbone, which is important for designing next generation DA CPs.

## 2. Results

### 2.1 Molecular design

In this study, two groups of polymers were purposefully designed to explore the influence of the side-chain structure on the single chain conformation of D–A CPs (as shown in Fig. 1). In the first group of DPP-based polymers, alkyl side chains with a systematically varied length were introduced to give the series DPP-T-C2CxCy, with  $x$  being 6, 8, 10, and 12, and  $y$  being 8, 10, 12, and 14 to denote the different lengths of the side chains based on the number of carbons, respectively. For the second series, alkyl side chains with systematically shifted branching points were designed to give the series IID-T2-CnC10C10, with  $n$  being 2, 3, 4, and 5 to denote the different positions of branching points based on the number of carbons. In this work, we combined experimental (SANS and UV-vis) and computational approaches (AA-MD simulation and DFT calculation) to understand the side chains' effect on backbone conformation and its relationship with optical absorption at a molecular level.

### 2.2 Probing single-chain conformation

The measurement of intrinsic single-chain conformation and optoelectronic properties of D–A CPs is challenging, as many D–A CPs tend to aggregate in solution.<sup>26</sup> Even for single chains, optical studies have revealed the occurrence of single-chain folding in oligomers above a critical molecular mass.<sup>44,45</sup> Thus, it is not easy to correlate the single-chain conformation with their optoelectronic properties. Moreover, previous work could also miss the existence of polymer aggregates in solution.<sup>46</sup> Here, we first perform temperature-dependent spectroscopy and scattering techniques to understand the solution state structure and aggregation behavior for both systems.<sup>24</sup>

Temperature-dependent UV-vis measurements were first conducted on DPP-based and IID-based polymer solutions to monitor aggregation behaviors by using the absorption spectra. As shown in Fig. 2a, b and S1,† all polymers formed aggregates at room temperature, given the additional low-energy absorption peak due to intrachain and interchain order.<sup>47,48</sup> In the heating process, UV-vis spectra exhibit a gradual blue shift (the absorption peak dropped from 850 nm to 700 nm for DPP-based polymers and from 710 nm to 620 nm for IID-based polymers). Meanwhile, the intensity of 0–1 and 0–0 transition peaks gradually decreases. The continuous decrease of the low-energy absorption features indicates that D–A polymer chains gradually disaggregate to single chains, resulting in a single and broad absorption peak above 140 °C.

Furthermore, we provided evidence for the disaggregation of DPP-based and IID-based polymers in solution by temperature-dependent NMR spectroscopy. Once forming aggregates, the protons in aggregates could not contribute to the <sup>1</sup>H NMR spectra due to the shielding effect.<sup>26</sup> Fig. 2c and d show the temperature-dependent <sup>1</sup>H NMR spectra of DPP-T-C2C6C8 and IID-T2-C2C10C10 polymers in *o*-DCB-*d*<sub>4</sub> (5 mg ml<sup>-1</sup>) (see Fig. S2† for the temperature-dependent <sup>1</sup>H NMR spectra of the other six polymers). The alkyl side chain's NMR peaks (1–5 ppm) are almost invisible at room temperature, indicating strong aggregates' formation. In contrast, well-defined alkyl NMR peaks at 1–2 ppm appeared above 120 °C and the peak intensity plateaued with further increased temperature, which confirms the complete dissolution of the polymers. We calculated the aggregation fraction at different temperatures by comparing the peak areas of alkyl peaks (1–5 ppm) with peak areas of fully dissolved polymers at 140 °C. As shown in Fig. 2e and f, the

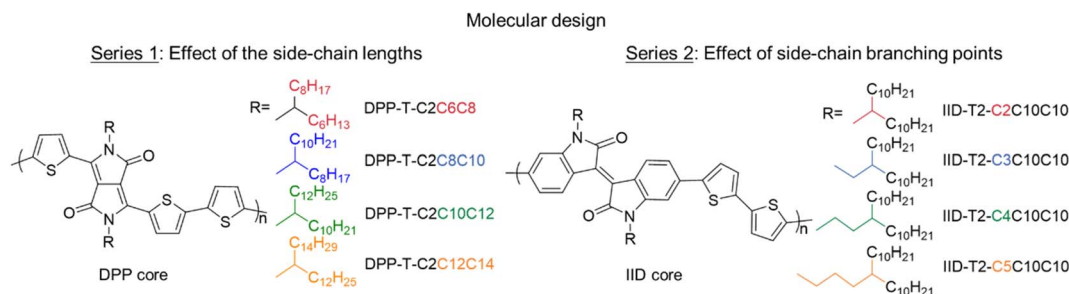


Fig. 1 Structure of DPP-based polymers with different side-chain lengths and IID-based polymers with different side-chain branching positions.

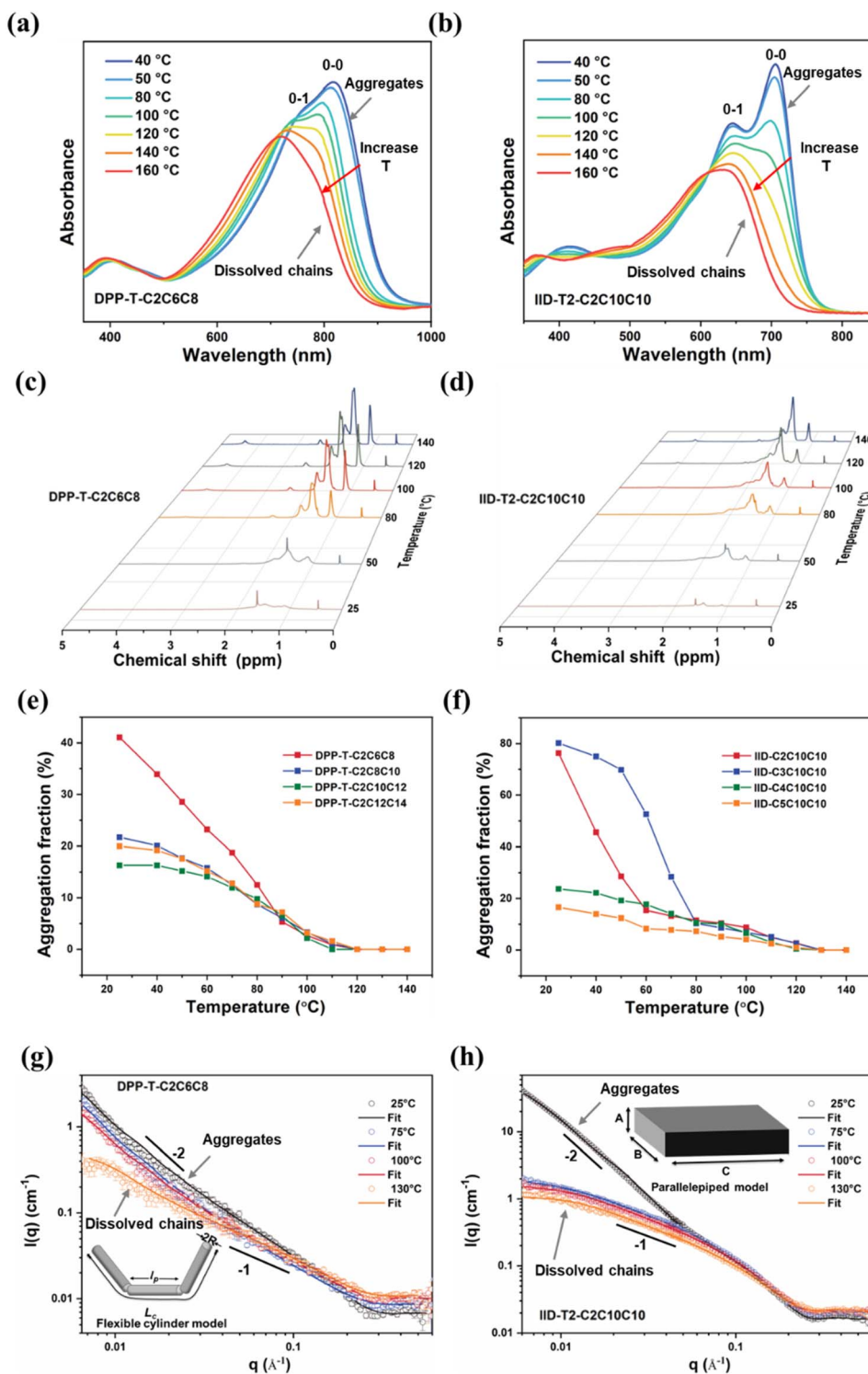


Fig. 2 Understanding the temperature dependent aggregation behavior of D–A CPs. Temperature-dependent UV-vis of DPP-T-C2C6C8 (a) and IID-T2-C2C10C10 (b) solutions in *o*-DCB ( $0.1 \text{ mg ml}^{-1}$ ). Temperature-dependent  $^1\text{H}$  NMR spectra of DPP-T-C2C6C8 (c) and IID-T2-C2C10C10 (d) polymer solutions in *o*-DCB- $d_4$ . Temperature-dependent aggregation fraction for DPP-T-C2C6C8 (e) and IID-T2-C2C10C10 (f) polymer solutions. The degree of aggregation was calculated by comparing the peak areas of alkyl peaks at different temperatures with the peak areas of fully dissolved polymers at  $140^\circ\text{C}$ . Temperature-dependent SANS curves for (g) DPP-T-C2C6C8 and (h) IID-T2-C2C10C10 polymer solutions. Lines are the best fitting *via* a suitable model. Embedded pictures are the flexible cylinder model and parallelepiped model.  $L_c$ ,  $l_p$ , and  $R$  are the contour length, persistence length, and radius of the flexible cylinder;  $A$ ,  $B$ , and  $C$  are the thickness, width, and length of the parallelepiped, respectively.

disaggregation process continues with the increase of solvent temperature. DPP-based polymers with a shorter side chain showed a higher aggregation fraction (about 40% at room temperature for DPP-T-C2C6C8 and 15–20% for DPP-T-C2C8C10, DPP-T-C2C10C12, and DPP-T-C2C12C14) due to the longer alkyl side chains that promote polymer's solubility. The branching position of alkyl side chains also affects the polymer's aggregation behavior. Moving the branching point away from the backbone reduces the aggregate content (from 80% for IID-T2-C2C10C10 and IID-T2-C3C10C10 to 20% for IID-T2-C4C10C10 and IID-T2-C5C10C10), indicating a significantly improved polymer solubility. The temperature required to fully dissolve DPP-based polymers and IID-based polymers is 120 °C and 130 °C, respectively.

Optical spectroscopic and NMR analyses confirmed the disaggregation but provided no information about the solution structure. Here, SANS measurements were then performed on solutions to monitor the change in the molecular conformation/polymer aggregates. At room temperature, as shown in Fig. 2g and h, the scattering signal from aggregates dominated the SANS profile, characterized by strong scattering intensity near the low scattering vector  $q$  region, which indicates that large aggregates over 50–100 nm were formed. Upon heating, the scattering intensity decreases in the low  $q$  region. A clear Guinier region in the low  $q$  range at 130 °C was observed for IID-T2-C2C10C10. However, the lowest  $q$  ( $\sim 0.006 \text{ \AA}^{-1}$ ) in this work is still not able to reach the Guinier regime of the polymer chain for DPP-T-C2C6C8 because of the higher molecular weight.

Next, we looked at the Kratky plots,<sup>49</sup> which can qualitatively assess the flexibility of polymers as shown in Fig. S3a† for DPP-T-C2C6C8 and Fig. S3b† for IID-T2-C2C10C10. Both fully dissolved polymers are semiflexible chains, as revealed by the high- $q$  upturn, while it should be a plateau for flexible polymer chains. A

power-law dependence of  $-1$  ( $0.01 \text{ \AA}^{-1} < q < 0.08 \text{ \AA}^{-1}$ ) suggests isolated rigid-rod like polymer chains (Fig. 2g and h). The SANS curves recorded at 130 °C for single chains were fitted with a flexible cylinder model (see the inset in Fig. 2g) in SasView,<sup>41</sup> which is a suitable model for semiflexible polymers with long alkyl side chains. The parameters extracted from the fitting of the SANS results are summarized in Tables 1 and 2. DPP-T-C2C6C8 has a radius of 1.1 nm, slightly smaller than that of IID-T2-C2C10C10 (1.3 nm). The results agree well with the difference in the side chain length. The  $l_p$  value of 16 nm for DPP-T-C2C6C8 and 16 nm for IID-T2-C2C10C10 were observed, which are about five times larger than that of P3HT ( $\sim 3$  nm).<sup>19,36,50</sup>

For SANS curves recorded below 130 °C, a combined model of a flexible cylinder model (for single chains) and parallelepiped model<sup>23</sup> (for aggregates, see the inset in Fig. 2h) was used. The details of the combined model are given in the ESI.† The scattering profile of DPP-T-C2C6C8 and IID-T2-C2C10C10 at room temperature and in the low- $q$  range has a larger slope ( $-2$ ) that indicates a sheet like aggregate (Fig. 2g and h). 2D plates were observed for DPP-T-C2C6C8 aggregates, with 1.5 nm thickness, 70 nm width, and 70 nm length. Upon heating, the aggregates gradually dissolved into single chains, as indicated by decreased  $A_1$  (the scaling factors corresponding to the volume fraction of aggregates). For IID-T2-C2C10C10 at 25 °C, the length of the aggregates is too large to be accurately estimated with the limited available  $q$  range. The cross section of the ribbon-like aggregates is about 10 nm in thickness and 45 nm in width. During heating, the size of aggregates significantly reduced from thousands of nm to tens of nm.

The featureless single-band UV-vis absorption peak, the high-resolution NMR spectra, and the appearance of the Guinier region above 130 °C directly prove that CPs form fully dissolved single chains in solutions. This important confirmation

**Table 1** Fitting parameters of temperature-dependent SANS curves for the DPP-T-C2C6C8 polymer.  $A_1$  and  $A_2$  are the scaling factors corresponding to the volume fraction of the particles<sup>a</sup>

	$A_1$	$A$ (nm)	$B$ (nm)	$C$ (nm)	$A_2$	$L_c$ (nm)	$l_p$ (nm)	$R$ (nm)
25 °C	0.7	$1.5 \pm 0.3$	$73 \pm 5$	$73 \pm 5$	1.5	$76 \pm 6$	$16 \pm 1$	$1.1 \pm 0.1$
75 °C	0.5	$1.5 \pm 0.1$	$69 \pm 2$	$69 \pm 2$	1.5	$76 \pm 6$	$16 \pm 1$	$1.1 \pm 0.1$
100 °C	0.3	$1.5 \pm 0.1$	$68 \pm 2$	$67 \pm 2$	1.5	$76 \pm 6$	$16 \pm 1$	$1.1 \pm 0.1$
130 °C	—	—	—	—	—	$76 \pm 6$	$16 \pm 1$	$1.1 \pm 0.1$

<sup>a</sup> Fitting parameters for dissolved polymers were obtained at 130 °C and fixed at other temperatures. See the ESI for the detailed discuss about our fitting models.

**Table 2** Fitting parameters of temperature-dependent SANS curves for the IID-T2-C2C10C10 polymer.  $A_1$  and  $A_2$  are the scaling factors corresponding to the volume fraction of the particles<sup>b</sup>

	$A_1$	$A$ (nm)	$B$ (nm)	$C$ (nm)	$A_2$	$L_c$ (nm)	$l_p$ (nm)	$R$ (nm)
25 °C	0.7	$9.6 \pm 0.1$	$45 \pm 2$	$3607 \pm 57$	2.9	$29 \pm 4$	$16 \pm 1$	$1.3 \pm 0.1$
75 °C	0.4	$2.1 \pm 0.2$	$4.2 \pm 0.2$	$60 \pm 6$	1.5	$29 \pm 4$	$16 \pm 1$	$1.3 \pm 0.1$
100 °C	0.3	$1.7 \pm 0.1$	$4.2 \pm 0.3$	$44 \pm 5$	1.2	$29 \pm 4$	$16 \pm 1$	$1.3 \pm 0.1$
130 °C	—	—	—	—	—	$29 \pm 4$	$16 \pm 1$	$1.3 \pm 0.1$

<sup>b</sup> Fitting parameters for dissolved polymers were obtained at 130 °C and fixed at other temperatures. See the ESI for the detailed discuss about our fitting models.

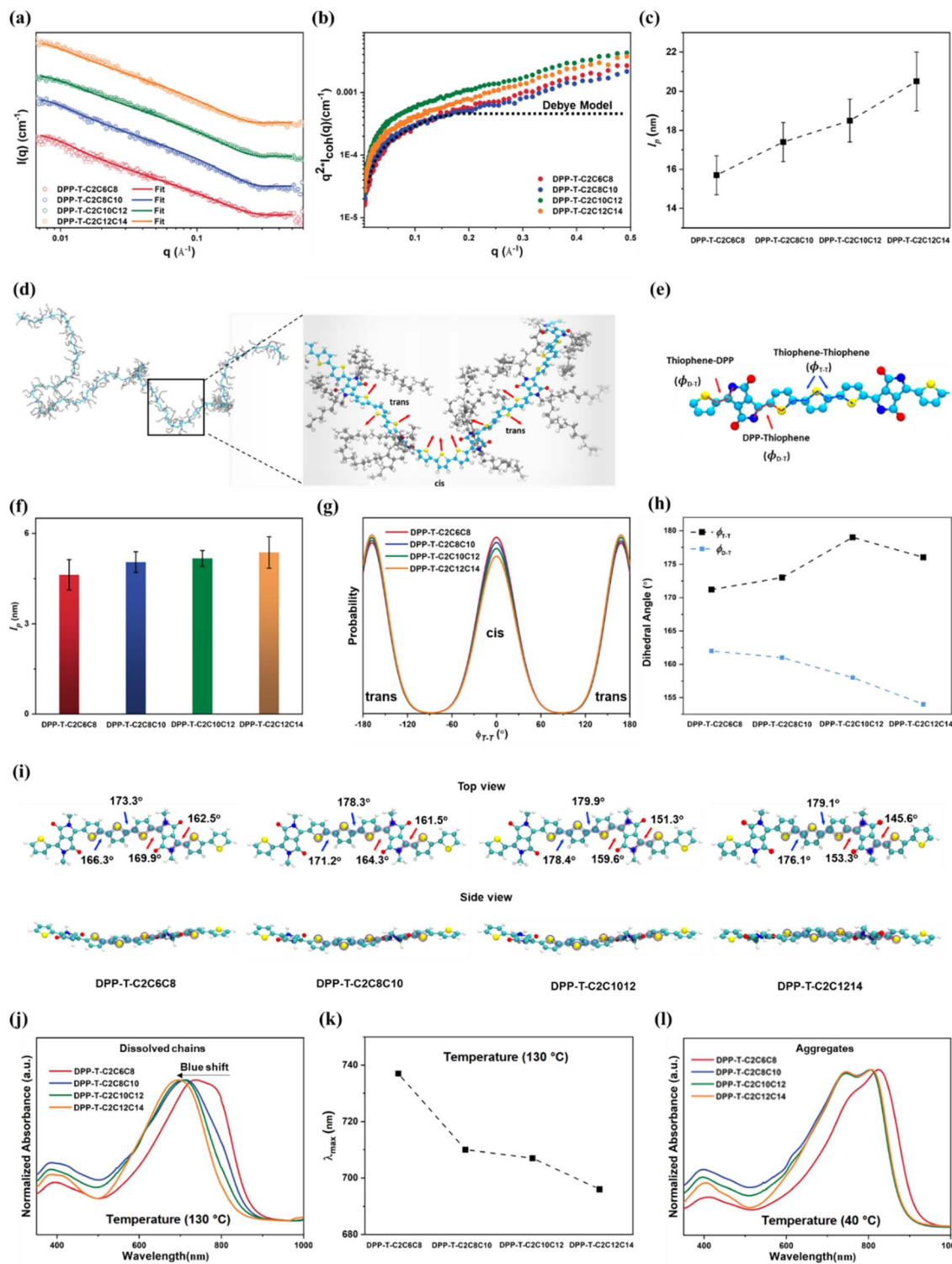


**Fig. 3** Single chain conformation of the DPP polymer: (a) SANS curves for DPP-based polymers in *o*-DCB-*d*<sub>4</sub> (5 mg ml<sup>-1</sup>) at 130 °C. Lines are the best fitting via a flexible cylinder model. (b) Kratky plots for DPP-based polymers. (c)  $l_p$  of DPP-based polymers with varied side-chain lengths. (d) A snapshot of a DPP polymer chain simulated by AA-MD simulation in a solution state. And the enlarged inset shows the two planar conformations: *trans* and *cis* conformations. (e) Schematic definition of the dihedral angles between thiophene–thiophene units ( $\phi_{T-T}$ ) and DPP–thiophene units ( $\phi_{D-T}$ ). (f)  $l_p$  of DPP-based polymers with varied side-chain length from MD simulation. (g) Thiophene–thiophene dihedral angle distributions from AA-MD simulation. (h) DFT calculated averaged  $\phi_{T-T}$  and  $\phi_{D-T}$ . (i) Optimized dimers with average torsional angles based on DFT calculations. Side view of energy-minimized conformers depicts the varying degrees of backbone coplanarity. (j) UV-vis spectra of DPP-based polymer solution, 0.1 mg ml<sup>-1</sup> in *o*-DCB at 130 °C. (k) The maximum absorption wavelength ( $\lambda_{max}$ ) of DPP-based polymers with varied side-chain lengths at 130 °C. (l) UV-vis spectra of DPP-based polymer solution, 0.1 mg ml<sup>-1</sup> in *o*-DCB at 40 °C (aggregated state).

of the single-chain state allows us to measure the molecular chain conformations for DPP-based and IID-based polymers in solution by SANS at 130 °C, and then explore the association between chain conformation and optical absorption.

### 2.3 Influence of the side-chain length on single-chain conformation and optical absorption

In this section, we explored how alkyl side-chain lengths (from 2-hexyldecyl to dodecylhexadecyl) influence the chain conformation and optoelectronic properties of DPP-based polymers. The SANS curves of DPP-based polymers with varied side-chain lengths are shown in Fig. 3a. Kratky plots (Fig. 3b) demonstrated that all four polymers are semiflexible chains. Thus, we used the flexible cylinder model to fit the SANS data, and the fitting parameters are listed in Table 3. The chain rigidity of DPP-based polymers increases with the side chain length, with  $l_p$  from 16 nm for DPP-T-C2C6C8 to 21 nm for DPP-T-C2C12C14 (see Fig. 3c and Table 3). We further employed AA-MD simulations to provide detailed insights into the chain conformation. A ribbon-like DPP polymer chain was observed from our simulations, as shown in Fig. 3d, which is the expected behavior for a polymer in a good solvent.<sup>51</sup> Two dihedral (*i.e.*, inter-ring torsion) angles are illustrated in Fig. 3e: the angle between the DPP-core and thiophene ( $\phi_{D-T}$ ) and the angle between two successive thiophene rings ( $\phi_{T-T}$ ). It should be mentioned that there are two planar conformational preferences: *trans* and *cis* conformations for the adjacent thiophene ring, as illustrated in Fig. 3e. For the *trans* conformation, the sulfur atoms on adjacent rings point in opposite directions. While both coplanar conformations preserve  $\pi$ -conjugation, the *cis* conformation induces backbone kinks, resulting in a lower chain rigidity. The  $l_p$  was defined as the characteristic length scale quantifying the directional correlation decay between adjacent backbone tangent vectors (Fig. S4†). The vectors connect the center-of-mass of adjacent functional groups (*i.e.*, thiophene ring and DPP-core) along the chain contour.<sup>52,53</sup> As shown in Fig. 3f, the predicted  $l_p$  of DPP-based polymers captures the same trend of SANS results despite the fact that different  $l_p$  values are observed, which might be attributed to the limitation of force field parameters (see the Method section).<sup>54</sup> Fig. 3g plots the probability distributions of defined dihedrals for the four polymers, which show a clear decrease in the population of *cis* conformations with increasing side-chain length. This indicates that the *trans* conformation is more energetically favorable for the polymer with a longer side-chain length, and thus is responsible for the observed higher  $l_p$  values. The probability

distributions for  $\phi_{D-T}$  show little change with increasing side-chain length (see Fig. S5†).

DFT calculation of structural and optical properties was further carried out on DPP dimers with periodical boundary conditions based on a 1-dimensional periodic model. In previous literature, the long alkyl side chains were replaced with the methyl group to save the DFT computational cost.<sup>32,55</sup> Therefore, the impact of the side chains on the torsion angle cannot be distinguished. Here, we include the whole alkyl side chains into the DFT model. The polymer's backbone is twisted as the dihedral angle deviates from 180°. As the side-chain length increases, the polymer backbone is more twisted (as indicated by the decrease in  $\phi_{D-T}$  from 162° to 152°, Fig. 3h). And it is more affected than  $\phi_{T-T}$  as it is closer to the branching point.<sup>56</sup> Geometry-optimized structures obtained by DFT calculation (Fig. 3i) show that the backbone adopts almost planar conformation but indeed more twist conformation with increasing side chain length.

Experimentally, there are small but systematic blue shifts of the absorption peak for fully dissolved DPP-based polymers with increasing alkyl chain length (from  $\lambda_{\max} = 737$  nm for DPP-C2C6C8 to  $\lambda_{\max} = 696$  nm for DPP-C2C12C14, as shown in Fig. 3j and k). Such blue shifts in optical absorption are consistent with backbone planarity change but are not correlated with the chain rigidity changes. The DFT calculated UV-vis spectra capture the blue shifts with increasing side chain length, as seen in Fig. S7.† However, at 40 °C, only the optical absorption of DPP-T-C2C6C8 solution showed a redshift compared with the other three polymers due to aggregates. This explains that the side chain length effect on the optical and electrical bandgap was not observed by UV-vis and cyclic voltammetry measurements on thin films in reported studies with the existence of aggregates.<sup>57–59</sup>

### 2.4 Influence of the branching position on chain conformation and optical absorptions

After understanding the side-chain length effect, a detailed analysis of the dependence of the conformation and optoelectronic properties on the position of the branching point was further explored, since the branch point is another commonly used strategy to design/optimize CPs. The SANS curves and Kratky plots for IID-based polymers are shown in Fig. 4a and b, and the  $l_p$  for IID-based polymers is shown in Fig. 4c and Table 4. A monotonic increase in the  $l_p$  from 16 nm for IID-T2-C2C10C10 to 19 nm for IID-T2-C5C10C10 was observed with moving the branching points farther away from the backbone. The MD simulation predicted  $l_p$  of IID-based polymers captures

**Table 3** Number averaged molecular weight ( $M_n$ ), dispersity ( $D$ ),  $\lambda_{\max}$  in solutions (130 °C), contour length ( $L_c$ ), persistence length ( $l_p$ ), and radius ( $R$ ) of DPP-based polymers

Polymer	$M_n$ (kg mol <sup>-1</sup> )	$D$	$\lambda_{\max}$ (nm)	$L_c$ (nm)	$l_p$ (nm)	$R$ (nm)
DPP-C2C6C8	88.5	4.09	737.0	76 ± 6	16 ± 1	1.1 ± 0.1
DPP-C2C8C10	76.6	3.27	710.0	69 ± 5	17 ± 1	1.1 ± 0.1
DPP-C2C10C12	60.6	2.44	707.0	52 ± 4	18 ± 1	1.2 ± 0.1
DPP-C2C12C14	61.8	2.97	696.0	60 ± 5	21 ± 2	1.2 ± 0.1

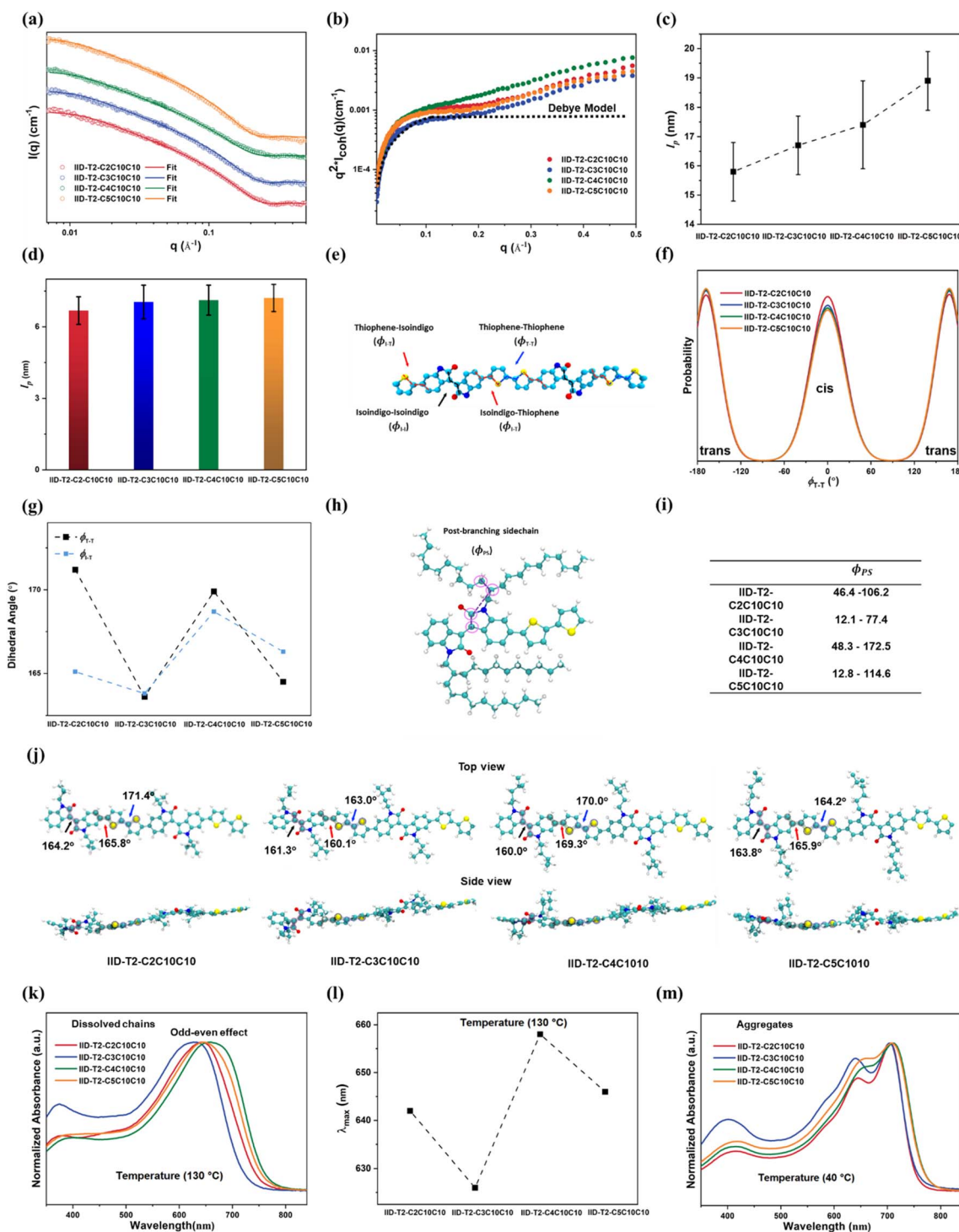


Fig. 4 Single chain conformation of the IID polymers: (a) SANS curves for IID-based polymers in *o*-DCB-*d*<sub>4</sub> (5 mg ml<sup>-1</sup>) at 130 °C. Lines are best fitting via the flexible cylinder model. (b) Kratky plots for IID-based polymers. (c)  $l_p$  of IID-based polymers with various side-chain branch positions. (d)  $l_p$  of IID-based polymers from MD simulation. (e) Schematic definition of the dihedral angles between thiophene–thiophene ( $\phi_{T-T}$ ) units, and isoindigo–thiophene ( $\phi_{I-T}$ ) units and isoindigo–isoindigo ( $\phi_{I-I}$ ) units. (f) Thiophene–thiophene dihedral angle distributions for IID-based polymers with varying side-chain branching positions from AA-MD simulation. (g) DFT calculated averaged  $\phi_{T-T}$  and  $\phi_{I-T}$ . (h) Repeating unit of a polymer chain showing the post-branching side chain dihedral angles. (i) Values calculated for the dihedral angles (in degrees). (j) Optimized dimers with average torsional angles based on DFT calculations. Side view of energy-minimized conformers depicts the varying degrees of backbone coplanarity. (k) UV-vis of IID-based polymer solution, 0.1 mg ml<sup>-1</sup> in *o*-DCB at 130 °C. (l)  $\lambda_{max}$  of IID-based polymers at 130 °C with various side-chain branching positions. (m) UV-vis of IID-based polymer solution, 0.1 mg ml<sup>-1</sup> in *o*-DCB at 40 °C.

**Table 4** Number averaged molecular weight ( $M_n$ ), dispersity ( $D$ ),  $\lambda_{\max}$  in solutions (130 °C), and contour length ( $L_c$ ), persistence length ( $l_p$ ) and radius ( $R$ ) of IID-based polymers

Polymer	$M_n$ (kg mol <sup>-1</sup> )	$D$	$\lambda_{\max}$ (nm)	$L_c$ (nm)	$l_p$ (nm)	$R$ (nm)
IID-T2-C2C10C10	20.6	1.76	642.0	29 ± 4	16 ± 1	1.3 ± 0.1
IID-T2-C3C10C10	19.8	1.45	626.0	30 ± 4	17 ± 1	1.4 ± 0.1
IID-T2-C4C10C10	31.2	2.14	658.0	32 ± 5	17 ± 2	1.4 ± 0.1
IID-T2-C5C10C10	31.7	2.19	646.0	34 ± 4	19 ± 2	1.5 ± 0.1

the same trend of SANS results (Fig. 4d). It is noticeable that as the branching position moves away from the backbone, a small but discernible preference towards *trans* configuration (*i.e.*, a decrease in the population of *cis* configuration) can be observed in Fig. 4f, which correlates well with the increased  $l_p$ . Also, the probability distributions for  $\phi_{1-T}$  do not change much with increasing spacer length between the branch point and backbone (see Fig. S10†).

DFT calculations of the backbone planarity were further performed. For IID-based polymers with an odd number of carbons of the spacer length between the branching point and backbone, the backbone is less planar compared with the even number of carbons of the spacer length (lower  $\phi_{1-T}$  and  $\phi_{T-T}$  in Fig. 4g, see Fig. 4e for the definition of dihedral angles). This difference is due to the different orientations of the side chains. For IID-T2-C2C10C10 and IID-T2-C4C10C10, the post-branching side chains orient out of the plane of the polymer backbone as indicated by the large  $\phi_{PS}$  (46°–106° for IID-T2-C2C10C10 and 48°–172° for IID-T2-C4C10C10, see Fig. 4h for this dihedral angle and values in Fig. 4i), from which significant steric hindrances between side chains can be avoided. In contrast, the post-branching side chains are oriented toward the co-facial area and pointed toward the backbone of the polymer in both IID-T2-C3C10C10 and IID-T2-C5C10C10, which is indicated by the values of  $\phi_{PS}$  12°–71° for IID-T2-C3C10C10 and 12°–114° for IID-T2-C5C10C10. Geometry-optimized structures obtained by DFT calculation (Fig. 4j) also showed that the backbone adopts more twist conformation for the even branching positions.

Experimentally, we also found that the UV-vis absorption spectra shift showed an odd–even effect<sup>60</sup> in terms of the branching point (see Fig. 4k and l) for fully dissolved single chains but not for aggregates (see Fig. 4m). This is in contrast with the trend of the optical bandgap and the electrical bandgap tested by using the thin-film samples, which do not show such an odd–even effect.<sup>39</sup> As can be seen in Fig. S12,† the recorded UV-vis spectra based on the optimized ground-state electronic structure of IID-based polymers capture the odd-even effect as experimental results. Such an odd-even effect in optical absorption is consistent with backbone planarity change but failed to be correlated with the chain rigidity changes. Previously, Liu *et al.*<sup>60</sup> have also observed that charge mobilities followed an odd–even relationship with respect to the branching positions for CPs based on the quinoidal *para*-azaquinodimethane (*p*-AQM) unit. Similarly, they found that at the odd branching points, the post-branching point chains oriented toward the polymer backbone, where the steric hindrance is disruptive to interchain packing.

### 3. Discussion

In this work, the detailed analysis of the NMR spectra, SANS, and optical spectra shows the critical role of alkyl side chains of D-A CPs beyond solubility. Three key observations are:

(a) Unsurprisingly, alkyl side chains significantly impact the solubility of CPs. Increasing the side-chain length or the spacer length between the branch point and backbone can increase the overall dimensions of side chains as the radius of the cylinder model ( $R$ ) increases as shown in Tables 3 and 4. The bulky side chains can hinder the inter-chain aggregation, which can be clearly seen in Fig. 2e and f.

(b) The intra-chain interaction between side chains influences the single-chain conformation. Increasing the bulkiness of side chains by increasing the side-chain length or spacer length rigidifies the polymer chain due to decreased population in *cis* conformation.

(c) Locally, alkyl side chains could also alter backbone planarity and optical absorption. Systematic blue shifts have been observed with increasing alkyl chain length. The optical shift changes according to an odd–even effect of the branching point. In both cases, the local backbone planarity is responsible for the optical shift.

Thus, we found that the optoelectronic properties of a given polymer depend on both the chain rigidity and more importantly local chain planarity. This loss of correlation between the optical bandgap and chain rigidity can be reconciled by the fact that factors that control the rigidity of polymer chains and conjugation length are not the same. The persistence length and conjugation length are both “subdivisions” for a long-chain molecule, as shown in Fig. 5. Within the persistence length, the polymer chain can be described as effectively rigid, purely from a polymer physics perspective. Thus, it is closely related to both the linearity and planarity of the polymer backbone. Despite preserving coplanar conformations, the *cis* conformation induces backbone kinks, which can be seen as breakers in  $l_p$  (see the schematics in Fig. 5). On the other hand, the conjugation length is the length scale on which the electron cloud can remain delocalized and communicated. This can be observed for absorption spectroscopy red shifts as the degree of polymerization increases with oligomers of conjugated polymers initially until it plateaued out. The polymer chain can be described as effectively planar within the conjugation length. Thus, within the rigid segment, the local backbone planarity determines the conjugation length as large twists of the conjugated backbone result in break of conjugation. Our DFT calculations indicate that the backbone of DPP-based and IID-

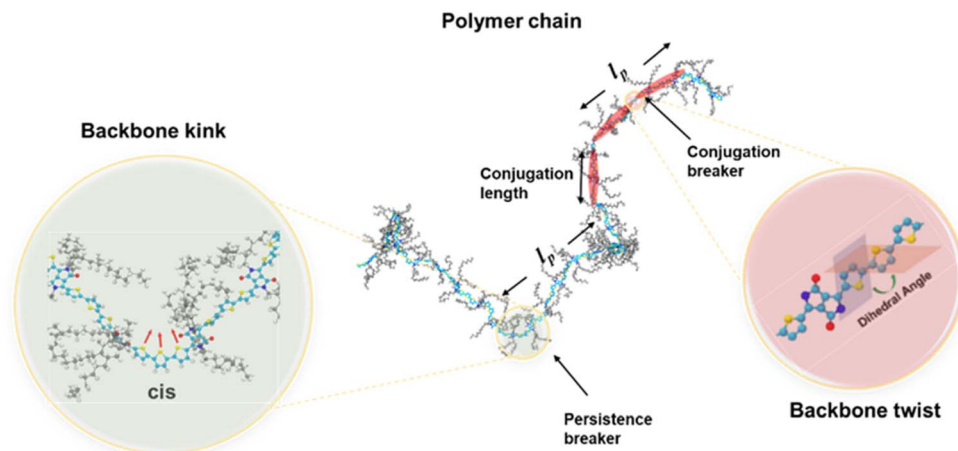


Fig. 5 Illustration of “subdivisions” for a long polymer chain, including persistence length ( $l_p$ ) and conjugation length. Backbone kinks limit the persistence length. Backbone twists limit the conjugation length.

based is not fully planar, despite being very rigid. And the optical shift can be well explained by the backbone local distortion. Previously, McCulloch and coworkers observed that both populated planar states (the *cis* and *trans* conformations) of P3HT can preserve conjugation, while *cis* conformations do not maintain the backbone correlations, which leads to a longer conjugation length than the persistence length for P3HT.<sup>36</sup> In contrast, for very rigid poly(phenylenevinylene) and polyfluorene, the conjugation length can be less than the persistence length,<sup>61–63</sup> due to unfavorable planar conformations. Ultimately, both chain rigidity and chain planarity jointly dictate the conjugation length and optoelectronic properties of conjugated systems.

## 4. Conclusions

In conclusion, we have investigated thoroughly how alkyl side chains affect the single chain conformation and optoelectronic properties of high-performance D–A CPs based on DPP and IID units. The chain rigidity of DPP-based and IID-based polymers increases with the bulkiness of side chains either by increasing the side-chain length or spacer length, owing to a decrease in the population of *cis* conformation between thiophene–thiophene building blocks. Although the chain rigidity of DPP-based polymers increases with alkyl chain lengths, blue shifts in optical absorption were observed. DFT calculation of the backbone planarity indicates that blue shifts can be attributed to a less planar backbone owing to stronger steric hindrance from longer side chains. For the IID polymer system with different branch points, an odd–even effect in the optical absorption spectrum was observed, ascribed to the coplanarity change of the polymer backbone due to the steric hindrance induced by side chains according to the DFT calculation. For the IID-based polymers with an odd number of carbons of the spacer length between the branch point and backbone, the alkyl side chains tend to be co-facial with the backbone plane and point toward the backbone, thus inducing stronger steric

hindrance. This work demonstrated the important effect of side chains on the molecular conformation of CPs backbone by combining experimental and computational approaches and illustrated this important molecular design consideration for future semiconducting polymer design.

## 5. Experimental

### 5.1. Materials and general methods

**5.1.1. Materials.** The synthetic details for DPP-based polymers<sup>64</sup> and IID-based polymers<sup>39</sup> are described in our previous studies. The polymers used here were synthesized following a similar synthetic procedure. The number average molecular weight ( $M_n$ ) and dispersity ( $\mathcal{D}$ ) (Tables 3 and 4) were determined relative to polystyrene standards at 160 °C in 1,2,4-trichlorobenzene (stabilized with 125 ppm of butylated hydroxytoluene) using an Agilent PL-GPC 220 High-Temperature GPC/SEC system equipped with four PLgel 10  $\mu\text{m}$  MIXED-B columns. Ortho-dichlorobenzene (*o*-DCB) and deuterated ortho-dichlorobenzene (*o*-DCB- $d_4$ ) ( $D > 99\%$ ) were purchased from Sigma Aldrich and used as received.

**5.1.2. UV-vis-NIR spectroscopy.** A Cary 5000 UV-vis-NIR spectrophotometer was used to record UV-vis-NIR spectra. Solution absorption data were acquired from *o*-DCB solution (0.1 mg ml<sup>−1</sup>) with temperatures ranging from 40 to 160 °C.

**5.1.3. Nuclear magnetic resonance (NMR).** Temperature-dependent <sup>1</sup>H-NMR spectra were recorded by using a Varian-500 MHz NMR spectrometer from 25 to 140 °C. Chemical shifts were reported in ppm relative to *o*-DCB- $d_4$  at 7.17 ppm (lower field peak) for <sup>1</sup>H-NMR.

**5.1.4. Small-angle neutron scattering (SANS).** SANS measurements were carried out on an Extended Q-Range Small-Angle Neutron Scattering Diffractometer (EQ-SANS) at the Spallation Neutron Source (SNS), Oak Ridge National Lab (ORNL).<sup>65</sup> The scattering wavevector used in this work ranged from 0.003 to 0.7  $\text{\AA}^{-1}$ , by using two different instrumentation configurations (4 m sample to detector distance with

a wavelength band of  $\lambda_{\min} = 12 \text{ \AA}$  and 2.5 m sample to detector distance with  $\lambda_{\min} = 2.5 \text{ \AA}$ ). Dilute solutions of DPP-based and IID-based polymers were prepared ( $5 \text{ mg ml}^{-1}$ ) in *o*-DCB- $d_4$ . The polymer solution samples were transferred into Hellma quartz cells with a 2 mm beam path length. Measurements were performed at 25 °C, 75 °C, 100 °C, and 130 °C, respectively. The solutions were equilibrated at each temperature for 40 min before measurements. Scattering data were reduced and corrected by subtracting the background from deuterated solvents and quartz cells. Absolute scattering intensity was obtained by using a standard porous silica sample.<sup>66</sup> Reduced data were also simultaneously fitted by using a suitable model in SasView to obtain chain conformation.<sup>41</sup>

## 5.2. Computational methods

**5.2.1. All-atomistic molecular dynamics simulations.** The initial configuration of atomistic DPPT and IID series molecular models was constructed using the Materials Studio platform. All MD simulations were carried out with the Large-scale Atomic/Molecular Massively Parallel Simulator (LAMMPS)<sup>67</sup> based on the Dreiding force-field (FF)<sup>68</sup> describing all bonded (stretching, bending, and torsional) and non-bonded interactions between atoms. The choice of the Dreiding FF functional forms is motivated by its simplicity coupled with a wide range of applicability in studying pure crystalline and pure amorphous phases of CPs.<sup>69</sup> To characterize the conformational changes in dilute solution, we consider a long single-chain polymer model having 60 monomers for both DPP-based and IID-based materials and take interactions between the polymer chain and solvent into account implicitly. For computational efficiency, the Lennard-Jones interaction potential (*i.e.*, non-bonded interaction) was truncated and shifted to zero at  $r_{\text{cut}} = 2^{1/6} \sigma$  for all the atoms to make the atom-atom interaction purely repulsive, hence mimicking good solvent conditions. All of the electrostatic contributions were computed from the coulombic pairwise interaction given by  $E = \frac{Cq_iq_j}{\epsilon r}$ , where  $C$  and  $\epsilon$  are an energy-conversion constant and the dielectric constant, respectively, and  $q_i$  and  $q_j$  are the charges on the atoms. Every single polymer was inserted into the cubic simulation cell with dimensions much larger than the initial chain length. Each system was first equilibrated for 1 ns under a canonical (NVT) ensemble (temperature was maintained by using a Nosé-Hoover thermostat<sup>70</sup> with a damping time constant of 50 fs), where the periodic boundary condition (PBC) was applied to all three directions with a time step of 1 fs. After equilibration, the simulations were subjected to a 100 ns production run in the NVT ensemble, and the data were collected every 20 ps to sample configurational trajectories adequately. The atomic configuration was depicted using Visual Molecular Dynamics (VMD).<sup>71</sup>

**5.2.2. Density functional theory.** DFT calculations are developed based on semi-local Perdew–Burke–Ernzerhof (PBE) functionals<sup>72</sup> to predict the chain conformation in the ground state, where we include the whole alkyl side chains into the DFT model. To avoid the finite chain-length effect, computational

models of the IID trimer and DPP dimer are developed based on a 1-dimensional periodic model.<sup>53</sup> The periodic model consists of three monomers in a vacuum where the solvent–polymer interaction was not considered, with the polymer backbone stretched in the *x*-direction. The *y*- and *z*-directions, which are perpendicular to the polymer backbone, are large enough to prevent interactions between images under the periodic boundary conditions. The size of the cell in this direction is chosen to minimize the total energy of the system. Then, the electronic structure is calculated through the solution of the self-consistent equation of DFT<sup>73</sup> via the Vienna *Ab initio* Simulation Package (VASP).<sup>74</sup> For the dihedral potential energy profile, the correlation consistent tripl-zeta basis set (cc-pVTZ)<sup>75</sup> was used in the rigid scan of the backbone's dihedral angles to obtain accurate predictions of energy barriers between conformers and potential energy surfaces.<sup>53</sup>

The absorption spectra for the geometrically optimized backbone of the IID trimer and DPP dimer were recorded by time-dependent DFT based on the CAM-B3LYP functional<sup>76</sup> and 6-31+G(d,p) basis set<sup>77</sup> using the Gaussian16 software package.<sup>78</sup> We used the polymer's ground structures for optical absorption calculations using time-dependent DFT (TD-DFT) and replaced the long side chains with methyl groups to improve the computational efficiency, as charge transport primarily occurs along the backbone.

## Author contributions

G. T. M., M. X., M. U. O., S. R. G., and T. L. synthesized the polymers. Z. C. performed the neutron scattering measurement, UV-vis measurement, and NMR measurement and analyzed the data. Z. L., S. A. T., A. A. and W. X. performed the MD simulation and DFT calculation. M. X. performed the UV-vis measurements on IID-based polymers. C. D. and K. H. assisted in neutron scattering measurement. X. G. conceive the idea of the project and directed and coordinated the overall investigation. Z. C., Z. L., and X. G. wrote the initial draft of the manuscript. All the authors revised and approved the manuscript.

## Conflicts of interest

There are no conflicts to declare.

## Acknowledgements

This work was supported by the U.S. Department of Energy, Office of Science, Office of Basic Energy Science under the award numbers of DE-SC0019361 and DE-SC0022050. S. R.-G. thanks the NSERC for financial support through a Discovery under award number RGPIN-2022-04428. Z. L., S. A. T., A. A. and W. X. acknowledge support from the U.S. National Science Foundation under NSF OIA Award No. 2119691 and the College of Engineering at North Dakota State University. T. L. thanks for the support of the National Key Research and Development Project (2022YFE0130600). This research used resources at the Spallation Neutron Source, a DOE Office of Science User Facility operated by the Oak Ridge National Laboratory. Part of the research was

conducted at the Center for Nanophase Materials Sciences, which is a DOE Office of Science User Facility.

## Notes and references

- H. Sirringhaus, N. Tessler and R. H. Friend, *Science*, 1998, **280**, 1741–1744.
- H. Huang, L. Yang, A. Facchetti and T. J. Marks, *Chem. Rev.*, 2017, **117**, 10291–10318.
- C. Wang, H. Dong, W. Hu, Y. Liu and D. Zhu, *Chem. Rev.*, 2012, **112**, 2208–2267.
- H. Luo, C. Yu, Z. Liu, G. Zhang, H. Geng, Y. Yi, K. Broch, Y. Hu, A. Sadhanala, L. Jiang, P. Qi, Z. Cai, H. Sirringhaus and D. Zhang, *Sci. Adv.*, 2016, **2**, e1600076.
- G. Li, R. Zhu and Y. Yang, *Nat. Photonics*, 2012, **6**, 153–161.
- W. Liu, S. Sun, L. Zhou, Y. Cui, W. Zhang, J. Hou, F. Liu, S. Xu and X. Zhu, *Angew. Chem., Int. Ed.*, 2022, **61**, e202116111.
- Y. Huang, E. J. Kramer, A. J. Heeger and G. C. Bazan, *Chem. Rev.*, 2014, **114**, 7006–7043.
- L. Lu, M. A. Kelly, W. You and L. Yu, *Nat. Photonics*, 2015, **9**, 491–500.
- Z. Yao, Y. Zheng, Q. Li, T. Lei, S. Zhang, L. Zou, H. Liu, J. Dou, Y. Lu, J. Wang, X. Gu and J. Pei, *Adv. Mater.*, 2019, **31**, 180747.
- A. Gumyusenge, X. Zhao, Y. Zhao and J. Mei, *ACS Appl. Mater. Interfaces*, 2018, **10**, 4904–4909.
- C. Yan, S. Barlow, Z. Wang, H. Yan, A. K.-Y. Jen, S. R. Marder and X. Zhan, *Nat. Rev. Mater.*, 2018, **3**, 18003.
- H. Wu, L. Ying, W. Yang and Y. Cao, *Chem. Soc. Rev.*, 2009, **38**, 3391–3400.
- J. Y. Oh, S. Rondeau-Gagné, Y. C. Chiu, A. Chortos, F. Lissel, G. J. N. Wang, B. C. Schroeder, T. Kurosawa, J. Lopez, T. Katsumata, J. Xu, C. Zhu, X. Gu, W. G. Bae, Y. Kim, L. Jin, J. W. Chung, J. B. H. Tok and Z. Bao, *Nature*, 2016, **539**, 411–415.
- J. C. Yang, J. Mun, S. Y. Kwon, S. Park, Z. Bao and S. Park, *Adv. Mater.*, 2019, **1904765**, 1–50.
- M. A. Alkhadra, S. E. Root, K. M. Hilby, D. Rodriguez, F. Sugiyama and D. J. Lipomi, *Chem. Mater.*, 2017, **29**, 10139–10149.
- A. C. Arias, J. D. Mackenzie, I. McCulloch, J. Rivnay and A. Salleo, *Chem. Rev.*, 2010, **110**, 3–24.
- S. Holliday, J. E. Donaghey and I. McCulloch, *Chem. Mater.*, 2014, **26**, 647–663.
- P. J. Flory, *Principles of Polymer Chemistry*, Cornell University Press, 1953.
- G. M. Newbloom, S. M. Hoffmann, A. F. West, M. C. Gile, P. Sista, H. K. C. Cheung, C. K. Luscombe, J. Pfaendtner and L. D. Pozzo, *Langmuir*, 2015, **31**, 458–468.
- P. Carbone and A. Troisi, *J. Phys. Chem. Lett.*, 2014, **5**, 2637–2641.
- C. L. Gettinger, A. J. Heeger, J. M. Drake and D. J. Pine, *J. Chem. Phys.*, 1994, **101**, 1673–1678.
- M. S. Vezie, S. Few, I. Meager, G. Pieridou, B. Döring, R. S. Ashraf, A. R. Goñi, H. Bronstein, I. McCulloch, S. C. Hayes, M. Campoy-Quiles and J. Nelson, *Nat. Mater.*, 2016, **15**, 746.
- C. Liu, W. Hu, H. Jiang, G. Liu, C. C. Han, H. Sirringhaus and D. Wang, *Macromolecules*, 2020, **53**, 8255–8266.
- Z. Cao, G. Ma, M. Leng, S. Zhang, J. Chen, C. Do, K. Hong, L. Fang and X. Gu, *ACS Appl. Polym. Mater.*, 2022, **4**, 3023–3033.
- J. J. Kwok, K. S. Park, B. B. Patel, R. Dilmurat, D. Beljonne, X. Zuo, B. Lee and Y. Diao, *Macromolecules*, 2022, **55**, 4353–4366.
- R. Steyrleuthner, M. Schubert, I. Howard, B. Klaumünzer, K. Schilling, Z. Chen, P. Saalfrank, F. Laquai, A. Facchetti and D. Neher, *J. Am. Chem. Soc.*, 2012, **134**, 18303–18317.
- P. J. Brown, D. S. Thomas, A. Köhler, J. S. Wilson, J. S. Kim, C. M. Ramsdale, H. Sirringhaus and R. H. Friend, *Phys. Rev. B: Condens. Matter Mater. Phys.*, 2003, **67**, 1–16.
- M. Xiong, X. Yan, J.-T. Li, S. Zhang, Z. Cao, N. Prine, Y. Lu, J.-Y. Wang, X. Gu and T. Lei, *Angew. Chem., Int. Ed.*, 2021, **60**, 8189–8197.
- M. Abdelsamie, T. P. Chaney, H. Yan, S. A. Schneider, I. A. Ayhan, E. D. Gomez, J. R. Reynolds and M. F. Toney, *J. Mater. Chem. A*, 2022, **10**, 2096–2104.
- Y.-Y. Zhou, Z.-Y. Wang, Z.-F. Yao, Z.-D. Yu, Y. Lu, X.-Y. Wang, Y. Liu, Q.-Y. Li, L. Zou, J.-Y. Wang and J. Pei, *CCS Chem.*, 2021, **3**, 2994–3004.
- Y. Xi, C. M. Wolf and L. D. Pozzo, *Soft Matter*, 2019, **15**, 1799–1812.
- S. P. O. Danielsen, C. R. Bridges and R. A. Segalman, *Macromolecules*, 2022, **55**, 437–449.
- D. Venkateshvaran, M. Nikolka, A. Sadhanala, V. Lemaury, M. Zelazny, M. Kepa, M. Hurhangee, A. J. Kronemeijer, V. Pecunia, I. Nasrallah, I. Romanov, K. Broch, I. McCulloch, D. Emin, Y. Olivier, J. Cornil, D. Beljonne and H. Sirringhaus, *Nature*, 2014, **515**, 384.
- Z. Cao, M. Leng, Y. Cao, X. Gu and L. Fang, *J. Polym. Sci.*, 2021, **60**, 298–310.
- M. Xiao, R. L. Carey, H. Chen, X. Jiao, V. Lemaury, S. Schott, M. Nikolka, C. Jellet, A. Sadhanala and S. Rogers, *Sci. Adv.*, 2021, **7**, eabe5280.
- B. McCulloch, V. Ho, M. Hoarfrost, C. Stanley, C. Do, W. T. Heller and R. A. Segalman, *Macromolecules*, 2013, **46**, 1899–1907.
- J.-H. Dou, Y.-Q. Zheng, T. Lei, S.-D. Zhang, Z. Wang, W.-B. Zhang, J.-Y. Wang and J. Pei, *Adv. Funct. Mater.*, 2014, **24**, 6270–6278.
- T. Lei, J.-Y. Wang and J. Pei, *Acc. Chem. Res.*, 2014, **47**, 1117–1126.
- T. Lei, J. H. Dou and J. Pei, *Adv. Mater.*, 2012, **24**, 6457–6461.
- B. Kuei and E. D. Gomez, *Soft Matter*, 2017, **13**, 49–67.
- D. R. Reid, N. E. Jackson, A. J. Bourque, C. R. Snyder, R. L. Jones and J. J. de Pablo, *J. Phys. Chem. Lett.*, 2018, **9**, 4802–4807.
- C. M. Wolf, L. Guio, S. Scheiwiller, V. Pakhnyuk, C. Luscombe and L. D. Pozzo, *ACS Polym. Au*, 2021, **1**, 134–152.
- N. E. Jackson, B. M. Savoie, K. L. Kohlstedt, M. Olvera, D. Cruz, G. C. Schatz, L. X. Chen and M. A. Ratner, *J. Am. Chem. Soc.*, 2013, **135**, 10475–10483.

- 44 Z. Hu, J. Liu, L. Simón-Bower, L. Zhai and A. J. Gesquiere, *J. Phys. Chem. B*, 2013, **117**, 4461–4467.
- 45 T. J. Fauvell, T. Zheng, N. E. Jackson, M. A. Ratner, L. Yu and L. X. Chen, *Chem. Mater.*, 2016, **28**, 2814–2822.
- 46 K. Zhao, Q. Zhang, L. Chen, T. Zhang and Y. Han, *Macromolecules*, 2021, **54**, 2143–2154.
- 47 Y. Liu, J. Zhao, Z. Li, C. Mu, W. Ma, H. Hu, K. Jiang, H. Lin, H. Ade and H. Yan, *Nat. Commun.*, 2014, **5**, 1–8.
- 48 W. Ma, G. Yang, K. Jiang, J. H. Carpenter, Y. Wu and X. Meng, *Adv. Energy Mater.*, 2015, **5**, 1–9.
- 49 W. D. Hong, C. N. Lam, Y. Wang, Y. He, L. E. Sánchez-Díaz, C. Do and W. R. Chen, *Phys. Chem. Chem. Phys.*, 2019, **21**, 7745–7749.
- 50 S. P. O. Danielsen, E. C. Davidson, G. H. Fredrickson and R. A. Segalman, *ACS Macro Lett.*, 2019, **8**, 1147–1152.
- 51 B. Kuei and E. D. Gomez, *Soft Matter*, 2017, **13**, 49–67.
- 52 H. P. Hsu, W. Paul and K. Binder, *Macromolecules*, 2010, **43**, 3094–3102.
- 53 J. Wildman, P. Repiščák, M. J. Paterson and I. Galbraith, *J. Chem. Theory Comput.*, 2016, **12**, 3813–3824.
- 54 C. M. Wolf, K. H. Kanekal, Y. Y. Yimer, M. Tyagi, S. Omar-diallo, V. Pakhnyuk, C. K. Luscombe, J. Pfaendtner and L. D. Pozzo, *Soft Matter*, 2019, **15**, 5067–5083.
- 55 F. He, C. Cheng, H. Geng, Y. Yi, Z. Shuai and A. Manuscript, *J. Mater. Chem. A*, 2018, **6**, 11985–11993.
- 56 L. Ning, G. Han and Y. Yi, *J. Mater. Chem. C*, 2019, **7**, 14198–14204.
- 57 B. C. Schroeder, T. Kurosawa, T. Fu, Y. C. Chiu, J. Mun, G. J. N. Wang, X. Gu, L. Shaw, J. W. E. Kneller, T. Kreouzis, M. F. Toney and Z. Bao, *Adv. Funct. Mater.*, 2017, **27**, 1–8.
- 58 R. Di Pietro, T. Erdmann, J. H. Carpenter, N. Wang, R. R. Shivhare, P. Formanek, C. Heintze, B. Voit, D. Neher, H. Ade and A. Kiriy, *Chem. Mater.*, 2017, **29**, 10220–10232.
- 59 M. Turbiez, D. M. De Leeuw, A. J. Janssen, J. C. Bijleveld, A. P. Zoombelt, S. G. J. Mathijssen, M. M. Wienk, M. Turbiez, D. M. de Leeuw and R. A. J. Janssen, *J. Am. Chem. Soc.*, 2009, **131**, 16616–16617.
- 60 X. Liu, B. He, A. Garzón-ruiz, A. Navarro, T. L. Chen, M. A. Kolaczowski, S. Feng, L. Zhang and C. A. Anderson, *Adv. Funct. Mater.*, 2018, **28**, 1801874.
- 61 H. Meier, U. Stalmach and H. Kolshorn, *Acta Polym.*, 1997, **48**, 379–384.
- 62 G. Klaerner and R. D. Miller, *Macromolecules*, 1998, **31**, 2007–2009.
- 63 G. Fytas, H. G. Nothofer, U. Scherf, D. Vlassopoulos and G. Meier, *Macromolecules*, 2002, **35**, 481–488.
- 64 S. Zhang, A. Alesadi, M. Selivanova, Z. Cao, Z. Qian, S. Luo, L. Galuska, C. Teh, M. U. Ocheje, G. T. Mason, P. B. J. St. Onge, D. Zhou, S. Rondeau-Gagné, W. Xia and X. Gu, *Adv. Funct. Mater.*, 2020, **30**, 1–9.
- 65 J. K. Zhao, C. Y. Gao and D. Liu, *J. Appl. Crystallogr.*, 2010, **43**, 1068–1077.
- 66 W. T. Heller, M. Cuneo, L. Debeer-Schmitt, C. Do, L. He, L. Heroux, K. Littrell, S. V. Pingali, S. Qian, C. Stanley, V. S. Urban, B. Wu and W. Bras, *J. Appl. Crystallogr.*, 2018, **51**, 242–248.
- 67 S. Plimpton, *J. Comput. Phys.*, 1995, **117**, 1–19.
- 68 S. L. Mayo, B. D. Olafson and W. A. Goddard, *J. Phys. Chem.*, 1990, **94**, 8897–8909.
- 69 O. Alexiadis and V. G. Mavrantzas, *Macromolecules*, 2013, **46**, 2450–2467.
- 70 S. Nosé, *Mol. Phys.*, 1984, **52**, 255–268.
- 71 W. Humphrey, A. Dalke and K. Schulten, *J. Mol. Graphics*, 1996, **14**, 33–38.
- 72 J. P. Perdew, K. Burke and M. Ernzerhof, *Phys. Rev. Lett.*, 1996, **77**, 3865–3868.
- 73 P. Hohenberg and W. Kohn, *Phys. Rev.*, 1964, **136**, B864–B871.
- 74 G. Kresse and J. Furthmüller, *Phys. Rev. B: Condens. Matter Mater. Phys.*, 1996, **54**, 11169–11186.
- 75 K. A. Peterson and K. E. Yousaf, *J. Chem. Phys.*, 2010, **133**, 174116.
- 76 C. Bannwarth and S. Grimme, *Comput. Theor. Chem.*, 2014, **1040–1041**, 45–53.
- 77 G. A. Petersson and M. A. Al-Laham, *J. Chem. Phys.*, 1991, **94**, 6081–6090.
- 78 M. J. Frisch, *et al.*, *Gaussian 09, Revision A. 1*, Gaussian, Inc., Wallingford, CT, 2009.